

# The relations between dust properties and galaxy global / integrated quantities in the nearby Universe

Bogdan A. Pastrav<sup>1</sup>\*

<sup>1</sup>*Astrophysics, Cosmology and Theoretical Physics Laboratory, Institute of Space Science-INFLPR Subsidiary, Atomistilor 409, 077125, Bucharest-Magurele, Romania*

Accepted xxxx xxxxxx xx. Received xx xxxxxxxx xx; in original form xxxx xxxxxxxx xx.

## ABSTRACT

Results of a case study of a sample of low-redshift galaxies are presented, to determine dust temperatures and emissivity indices through a less time-consuming method, and to connect both global and integrated galaxy properties with those of dust, ISM and star-formation. Dust temperatures ( $T_d$ ) are determined based on the corresponding galaxy dust masses, independently calculated in our previous work, through a self-consistent method, without the need to actually perform a complete spectral energy distribution (SED) fit of the cold dust emission fluxes. The range and average dust temperatures are found to be consistent within errors with values from other studies. Simultaneously, the dust emissivity indices ( $\beta_d$ ) are determined, and their evolution with temperature quantified, with the  $T_d$  anti-correlation still being present. It is investigated whether  $\beta_d$  can be predicted from other relation or if it scales with other integrated dust / ISM or galaxy property, which could be used as a proxy. In this respect, new and established relations between  $T_d$ ,  $\beta_d$ , the dust surface density and global / integrated galaxy and star-formation related quantities are presented and analysed. We find that SFR, sSFR or  $\Sigma_{SFR}$  are inconclusive traces of the dust temperature. We also find that the extent of dust emission distribution is slightly lower on average, but comparable with the optical stellar continuum emission one. The results and conclusions can be relevant for larger scales studies of low to mid-redshift galaxies from the latest surveys.

**Key words:** ISM: dust, extinction – ISM: evolution – galaxies: evolution – galaxies: star formation – infrared: galaxies – galaxies: ISM

## 1 INTRODUCTION

Dust has a central role in galaxy evolution and star-formation, regulating many processes in the interstellar medium (ISM) of galaxies, as it absorbs and scatters more than one third up to half of the ultraviolet (UV) radiation coming from young and old stars alike (Driver et al. 2007; Bendo et al. 2014; Bianchi et al. 2018), and radiates it at longer wavelengths - near-infrared (NIR) to sub-millimetre (Draine 2003; Galliano et al. 2018). It is a catalyst for molecular hydrogen formation and, as dust grains are composed mainly of metals, has a direct influence on the metallicities of galaxies. Dust grains of different sizes show different ranges in temperatures (Li & Draine 2001) - small grains suffer stochastic heating from star-forming regions, with huge variations in temperature (to very high values, from 100K up to 1000K), while large grains are in a state of relative thermal equilibrium with the interstellar radiation field (having temperatures in the range 10-35K), emit mostly in the infrared, and constitute the dominant component of the total dust mass within galaxies (Vlahakis et al. 2005) and of the FIR total flux (Draine & Li 2007).

Determining the dust properties - mainly the dust mass, dust temperature and its emissivity index, can be a challenging task if

not enough NIR to far-infrared (FIR) and sub-mm photometric data are available to fully sample the spectral energy distribution of the dust. These properties are pivotal in studies of star-formation (to determine how much dust is obscuring the star-formation regions) and interstellar medium evolution. The dust emissivity index (also known as dust mass absorption coefficient) is essential when deriving dust masses from spectral energy distribution fits of the cold dust emission, but it is also a parameter tightly connected to the properties of dust grains, such as their composition (the proportion of silicates vs graphite) and structure (crystalline or amorphous), and the dust temperature. In most theoretical models the dust emissivity index has been fixed to a value  $\beta_d = 2$  (e.g. Weingartner & Draine 2001; Draine 2003), but from observations its value was not accurately and reliably constrained as one needs available data in the Rayleigh-Jeans part of the cold dust SED, and therefore available sub-mm and millimetre data. The average observational values measured for nearby galaxies and the Milky Way range between 0.8 and 2.5 (Yang & Phillips 2007; Paradis et al. 2010; Juvela et al. 2011; Boselli et al. 2012; Galametz et al. 2012; Smith et al. 2012; Clemens et al. 2013; Rémy-Ruyer et al. 2013; Cortese et al. 2014; Galametz et al. 2014; Planck Collaboration 2014; Grossi et al. 2015; Planck Collaboration 2015; Tabatabaei et al. 2014; Lamperti et al. 2019; Bendo et al. 2024).

To determine the dust mass, temperature and its mass absorption

\* E-mail: bapastrav@spacescience.ro

coefficient, a routinely used single-temperature modified black-body (MBB) has been proven to describe quite well the cold dust SED at wavelengths above  $\sim 100\mu\text{m}$ , for regions in our own Galaxy, in nearby Universe but also for high-redshift galaxies (e.g. [Paradis et al. 2010](#); [Skibba et al. 2011](#); [Bianchi 2013](#); [Pozzi et al. 2020](#); [Tang et al. 2021](#); [Witstok et al. 2022](#); [Algera et al. 2024](#)), for most cases where the optically thin approximation is valid ([Eales & Edmunds 1996](#)). To extract these three parameters from SED fits for large samples is computationally expensive and in many studies, sometimes the dust mass absorption coefficient was constrained to a value  $\beta_d = 2$  (e.g. [Dunne et al. 2000](#); [Vlahakis et al. 2005](#); [Skibba et al. 2011](#); [Hunt et al. 2015](#)). However, it was been observed that a single temperature for the whole dust distribution is not adequate for all galaxies, and therefore two MBB were used, one for each of warm and cold dust components ([Dunne & Eales 2001](#); [Vlahakis et al. 2005](#); [Galametz et al. 2012, 2014](#); [Kirkpatrick et al. 2014](#); [Tabatabaei et al. 2014](#)), resulting in dust masses approximately twice higher than before. As variations in  $\beta_d$  between and within galaxies were observed, in other works it was left as a free parameter in the SED fitting procedure ([Boselli et al. 2012](#); [Galametz et al. 2012](#); [Smith et al. 2012](#); [Clemens et al. 2013](#); [Rémy-Ruyer et al. 2013](#); [Cortese et al. 2014](#); [Tabatabaei et al. 2014](#); [Galametz et al. 2014](#); [Kirkpatrick et al. 2014](#); [Grossi et al. 2015](#); [Lamperti et al. 2019](#); [Bendo et al. 2024](#)). Still, the use of a single MBB is a simplification of dust emission treatment, and the output parameters can be looked as apparent or effective temperatures and emissivity indices, as there is a mix of warm and dust components along the line of sight, with various size distributions, grain compositions and therefore, grain emissivities. The dust masses however, are more robust quantities, not so much affected by the use of free or fixed  $\beta_d$  ([Cortese et al. 2014](#)). Nevertheless, this method provides meaningful results and can help us investigate and understand the variations of dust properties with other galaxy and star-formation relevant global parameters.

This is the fourth paper of the series, following from [Pastrav \(2020\)](#) (Paper I, where we focused on dust effects on disc scaling relations), [Pastrav \(2021\)](#) (Paper II, where the main bulge and early-type galaxy scaling relations were analysed, together with black-hole scaling relations and criteria for bulge and galaxy classification) and [Pastrav \(2024\)](#) (Paper III, where we concentrated on the star-formation and dust/ISM scaling relations and deriving more instantaneous dust-corrected star-formation rates (SFR) using unattenuated  $H\alpha$  luminosities).

Here, the goal of this case study is to: a) derive accurate dust temperatures and corresponding dust emissivity indices for the same galaxies analysed in Papers I and III (for consistency and validation of the method), using previous work prescriptions and the dust masses independently (of this study) derived in Paper I, through a self-consistent approach; b) investigate the  $T_d - \beta_d$  evolution and its potential degeneracy; c) check for possible tracers for the dust temperature among the star-formation related quantities, that could be used to estimate  $T_d$  and  $\beta_d$  when there are not enough photometric data available to extract these from a spectral energy distribution (SED) fit; d) investigate / analyse the relations - new or confirmed - between  $\Sigma_d, \beta_d$ , metallicity ( $Z[O/H]$ ), SFR, their implications for star-formation and ISM evolution, and which correlations are tighter and fundamental. A widely used modified blackbody function (MBB) - dependent on  $T_d, \beta_d$  and frequency ( $\nu$ ), is considered to characterise the cold dust emission SED in the NIR-submm wavelength range. While for this single temperature dust emission SED usually multiple fluxes / luminosities are needed at various wavelengths in the specified range (and sometimes not available) to derive the dust

masses through SED fitting (and subsequently the dust temperatures and emissivity indices), through this present approach only the flux / luminosity at  $250\mu\text{m}$ , characteristic for the peak of the cold dust emission, is required, while  $\beta_d$  is left as a free parameter. Thus, the whole cold dust emission SED will not be fitted (less computationally expensive) because the dust masses for this sample are apriori known (from Paper I, or could be calculated for other samples of galaxies using the method presented in the same paper) and independently derived. For some of the conclusive corrected relations we investigate the degree of correlation between the parameters (where relevant), calculate the scatter of these relations and analyse the implications of the main results for ISM evolution and star-formation. We then discuss these results and compare with other relevant studies on low-redshift galaxies.

The procedure described in this paper can be used in conjunction with the method to derive dust masses from Paper I (and potentially the prescriptions to derive SFR from Paper III) in larger scale studies of ISM evolution and star-formation, if needed and suitable optical+FIR photometry data are available.

The paper is organised as follows. In Sect. 2 we present briefly the galaxy sample used in this study, while in Sect. 3 we describe the method used for the determination of dust temperature and dust emissivity index. In Sect. 4 we present the main results - the relations between  $T_{\text{dust}}, \beta_d$ , the surface density of dust, the star-formation or stellar mass, and other related global and integrated quantities, together with all their characteristic parameters. In Sect. 4.5 we show how the extent of dust distribution compares with the optical stellar emission one. The results are discussed in relation with other relevant studies in the literature. In Sect. 5 we discuss upon the possible sources of errors, differences with other studies, and the limitations of the method, while in Sect. 6 we summarise the important results obtained in this study and draw some conclusions.

## 2 SAMPLE

Our sample of 24 nearby galaxies - the same as in [Pastrav \(2024\)](#), is used as case study for consistency of the analysis and validation of the method. It comprises 19 low-redshift spiral galaxies and 5 lenticulars, included in the SINGS (*Spitzer* Infrared Nearby Galaxies Survey; [Kennicutt et al. 2003](#)) survey and the KINGFISH project (Key Insights on Nearby Galaxies: a Far-Infrared Survey with *Herschel*; [Kennicutt et al. 2011](#)). The galaxies were already analysed in B band in Paper I and Paper II, while in Paper III the images of the galaxies were analysed at the  $H\alpha$  line wavelength. As before, we did not consider barred, dwarf and irregular galaxies from the KINGFISH sample, because we want to observe dust-free scaling relations, and at this point we cannot properly account for the effects of dust on the photometric and structural parameters of the former (barred galaxies), or for the more peculiar geometry of the latter (dwarfs and irregulars). Ellipticals from the KINGFISH survey are also not considered as we focus here on more dusty galaxies to derive the dust characteristics ( $T_d$  and  $\beta_d$ ) and their relation with star-formation and dust/ISM relevant quantities.

More details about the galaxy images and their characteristics are given in Papers I, II and III, and therefore we do not repeat them here. The KINGFISH project is an imaging and spectroscopic survey, consisting of 61 nearby ( $d < 30$  Mpc) galaxies, chosen to cover a wide range of galaxy properties (morphologies, luminosities, SFR, etc.) and local ISM environments typical for the nearby Universe, being therefore representative for the population of typical low redshift galaxies.

### 3 METHOD

Dust temperatures are determined based on the galaxy dust masses previously calculated in [Pastrav \(2020\)](#) through a self-consistent method. The details are given below. The star-formation rates and related quantities (specific star-formation rates - sSFR, SFR surface density -  $\Sigma_{SFR}$ ), both observed and intrinsic, which appear in some of the investigated relations in this study, have also been determined previously in Paper III (see Table 4 for numerical values and Section 3 for the method) from integrated H $\alpha$  luminosities and previous work prescriptions and relations.

#### 3.1 Deriving dust temperature and dust emissivity index

For a better understanding, we first remind the reader very briefly what relations were used to derive the dust masses for the whole sample,  $M_d$ , in Paper I (see there section 3.3). Prior to deriving dust masses, the empirical correlation between central face-on dust opacity in the B band ( $\tau_B^f$ ) and the stellar mass surface density ( $\mu_*$ ) of nearby spiral galaxies, found by [Grootes et al. \(2013\)](#) (Eq. 1), was used to determine the  $\tau_B^f$  values. This quantity was essential when applying the corrections for dust effects for all photometric and structural parameters, but also for the subsequent determination of dust masses, using Eqs. (2) and (A1-A5) from [Grootes et al. \(2013\)](#). We show this below in Eq. 2. This relation is based on the fixed large scale star-dust geometry of the [Popescu et al. 2011](#) model, where the diffuse dust in the disk (which mostly determines the optical depth of a spiral galaxy) is considered to have an axisymmetric distribution, as two exponential discs (see also Eq. (44) in [Popescu et al. 2011](#)).

$$\log(\tau_B^f) = 1.12(\pm 0.11) \cdot \log(\mu_*/M_\odot kpc^{-2}) - 8.6(\pm 0.8) \quad (1)$$

$$\tau_B^f = K(B) \frac{M_d}{R_{s,d}^2(B)} \quad (2)$$

where  $K(B)$  is a constant containing the details of the dust geometry and dust spectral emissivity ( $k_\nu$ ) of the [Draine \(2003\)](#) model at the B band wavelength, while  $R_{s,d}(B)$  represents the observed B band scale-length of the stellar disc (obtained in Paper I). All the values of  $M_d$ ,  $R_{s,d}(B)$ ,  $\tau_B^f$  and  $\mu_*$  are tabulated in Tables 2 & 3 from Paper I.

To characterise the dust emission spectral energy distribution in the NIR-submm range (above 70-100 $\mu m$ ) - the cold dust emission SED, and considering the dust grains to be in local thermal equilibrium, we use a modified blackbody function as in the following relation. This is because it was shown in many studies (see the references in Sec. 1) that it approximates quite well this part of a galaxy SED, in the optically thin limit. It is still an oversimplification does not take into account that dust within a galaxy most likely has a range of dust temperatures (different dust heating sources, e.g. [Bendo et al. 2014](#)) and therefore multiple dust components with different grain sizes along the line of sight. Nevertheless, meaningful conclusions about the overall dust temperature and dust grain sizes (through the derived  $\beta_d$  value) can be extracted from such fits. We explain in Sect. 5 why using two MBB functions (one for each of the warm and cold dust components) is not feasible in this study, with the present approach.

$$F_\nu = \frac{M_d}{d_{gal}^2} \kappa_\nu B(\nu, T_d) = \frac{M_d}{d_{gal}^2} \kappa_{\nu_0} \left(\frac{\nu}{\nu_0}\right)^{\beta_d} B(\nu, T_d), \quad (3)$$

where  $F_\nu$  is the observed flux density at the frequency  $\nu$ ,  $d_{gal}$  is the distance to the galaxy,  $\kappa_{\nu_0}$  represents the dust mass absorption coefficient at the frequency  $\nu_0$ , while  $\beta_d$  is the dust spectral emissivity

index (it gives the variation of the dust mass absorption coefficient with  $\nu$ ; [Eales & Edmunds 1996](#))

$$\kappa_\nu = \kappa_{\nu_0} \left(\frac{\nu}{\nu_0}\right)^{\beta_d} \quad (4)$$

For this study, our choice is to use the flux density at  $\lambda = 250\mu m$ , a data point far enough in the IR on the SED (and therefore not affected by dust) which constrains / characterises well the peak of the cold dust emission and is dominated by the thermal emission of the cold dust. The flux density at 250 $\mu m$  was also used in [Dale et al. \(2012\)](#) and [Grootes et al. \(2013\)](#) to derive dust masses, while [Galametz et al. \(2012\)](#) and [Skibba et al. \(2011\)](#) considered the flux densities at  $\lambda = 500\mu m$ , which is known to be less sensitive at variations of the dust temperature. For  $\nu_0$  we use the value corresponding to  $\lambda_0 = 100\mu m$ , while for  $\kappa_{\nu_0}$  we take the value at  $\lambda_0$  from [Draine \(2003\)](#). As pointed out by [Bianchi \(2013\)](#), using a  $\kappa_{\nu_0}$  value derived from a dust model that uses a certain fixed value for dust spectral emissivity index ( $\beta_d = 2$  as in the case of the [Draine 2003](#) model) to directly derive dust masses introduces an important bias, when  $\beta$  is a variable parameter. However, we will show in the following that this is not really the case in this study.

We consider here two scenarios - one in which  $\beta_d$  is a free parameter, while in the second one we fix the dust emissivity index to a value  $\beta_d = 2$ , just as in other works. This is done with the purpose of illustrating the differences that appear in the dust temperatures and the mean values of the sample, but also to investigate how fixing  $\beta_d$  can influence some of the relevant scaling relations involving dust temperature and SFR quantities. Thus, to determine the best-fit values for  $(T_d, \beta_d)$  we start for each galaxy with two sets of test values for  $k_\nu$  and  $T_d$  in Eq. 3:  $k_\nu = [0., \dots, 10.] m^2/kg$  in steps of  $0.05 m^2/kg$  and  $T_d = [0., \dots, 80.] K$  in steps of  $0.1 K$ . In the first step, we determine the best-fit value for  $T_d$  that minimises the difference between the dust mass independently derived from Eq. 2 and the one determined using Eq. 3 (the minimum of the  $\chi^2$  function) considering the entire range of values for  $k_\nu$  and  $T_d$ . With this best-fit value of the dust temperature -  $T_d^{fit}$ , in the second step, a best-fit blackbody function  $B(\nu, T_d^{fit})$  is introduced now in Eq. 3, and a corresponding best-fit  $k_\nu$  value is determined,  $k_\nu^{fit}$ . Finally, we derive the dust emissivity index for each galaxy,  $\beta_d$ , using  $k_\nu^{fit}$  and Eq. 4. In the second scenario,  $\beta_d = 2$  is fixed from the start, and using the same procedure we determine corresponding best-fit values for the dust temperature,  $T_d^{bfix}$ . This procedure is similar with a grid method, to determine dust temperature values without considering any particular value for the dust emissivity index. This kind of procedure should reduce spurious correlations between  $T_d$  and  $\beta_d$ . The consideration of a free  $\beta_d$  was likewise used in other studies on NIR-FIR-submm data - e.g. [Boselli et al. \(2012\)](#), [Galametz et al. \(2012\)](#), [Smith et al. \(2012\)](#), [Clemens et al. \(2013\)](#), [Cortese et al. \(2014\)](#), [Rémy-Ruyer et al. \(2013\)](#), [Tabatabaei et al. \(2014\)](#), [Galametz et al. \(2014\)](#), [Kirkpatrick et al. \(2014\)](#), [Grossi et al. \(2015\)](#), [Lamperti et al. \(2019\)](#), [Bendo et al. \(2024\)](#).

Now, coming back to the issue of using a fixed  $\kappa_{\nu_0}$  derived from a dust model calibrated on a fixed value of  $\beta_d$ , and following the procedure described above, one can see that the potential bias introduced cancels out. First, this issue appeared in other studies when trying to derive *temperature-dependent* dust masses from SED fits (together with  $T_d$  and  $\beta_d$ ) while here we already have these masses derived -  $M_d$ . Second,  $\kappa_{\nu_0}$  is present in both terms of the minimising function, in both dust mass expressions from Eqs. 2 (embedded in the value of  $K(B)$ ) & 3, and therefore when looking for the best-fit value for  $T_d$  that minimises the differences,

its biasing effect is effectively cancelled. This is common for both analysed scenarios - variable and fixed  $\beta_d$ .

We also determine here the observed dust mass surface density,  $\Sigma_d^{obs}$  essential in some of the investigated relations, using the observed dust disc scalelength,  $R_s^{dust}$ . As the diffuse dust is also considered to be distributed just as stars in an exponential disc following Popescu et al. (2011) model, the latter is determined from the relation

$$R_s^{dust} = (M_d \kappa_v(B) / 2\pi \tau_B^f)^{1/2} \quad (5)$$

with  $\kappa_v(B) = 2.46228 pc^2 / M_\odot$  (dust mass absorbtion coefficient in B band) calculated from Draine (2003) model and their data tables, while for  $\Sigma_d$  we have

$$\Sigma_d = M_d / 2\pi (R_s^{dust})^2 \quad (6)$$

For two galaxies - NGC0024 and NGC4450 - dust temperatures and emissivity indices could not be derived as needed fluxes at  $250\mu m$  could not be identified in the literature / databases, even though their dust opacities, dust masses and star-formation rates were calculated in Papers I and III.

### 3.2 Observed and corrected (intrinsic) dust properties

Here we have to mention that in the following plots from Sect. 4 and in Table 1, one will see two sets of values for dust temperatures (in both scenarios - with  $\beta_d$  variable or fixed), for  $\beta_d$ , and also for  $R_s^{dust}$ . For the dust temperatures and emissivity indices, this may be counterintuitive. The explanation for this stands in the way these quantities are derived and the relations used in this process. Thus, dust temperatures are derived, as already metioned, based on dust masses independently derived through a self-consistent method in Paper I. One can see that the relations used for this purpose - Eq. 1 & 2, have quantities that depend on the observed B band disc scalelength,  $R_{s,d}$ , which is affected by dust, projection and decomposition effects (Pastrav et al. 2013a,b). As a consequence, this resulted in two sets of values for dust masses,  $M_d$  and  $M_d^i$ , the observed (measured) and intrinsic (corrected) ones. Therefore, when applying the grid-like method described in Sect. 3.1 and the minimisation function, one will obtain two sets of values for the best-fit dust temperature,  $T_d^{fit}$ , one for each of  $M_d$  and  $M_d^i$ . We call these observed and intrinsic dust temperatures,  $T_d$  and  $T_d^i$ . This will create two different best-fit blackbody functions for each of these temperature values, and following the other steps of the procedure, two dust emissivity index values -  $\beta_d$  &  $\beta_d^i$ . According with the naming pattern already used, we call these *observed* and *intrinsic* (corrected) dust emissivity indices. For the same reasons, we have two sets of dust disc scalelengths as well,  $R_s^{dust}$  &  $R_s^{dust,i}$ , as these are determined based on dust masses -  $M_d$  and  $M_d^i$ .

In the following section, we shall see from the plots and fits that there are some non-negligible differences for some relations and their characteristic parameters when considering both sets of values for  $T_d$  and  $\beta$ .

To calculate the intrinsic (corrected) dust surface densities,  $\Sigma_d^i$  we use a similar formula as in Eq. 6 as follows

$$\Sigma_d^i = M_d^i / 2\pi (R_s^{dust,i})^2 \quad (7)$$

where  $M_d^i$ , the intrinsic dust masses of the galaxies, were previously derived in Paper I (see Table 2), and

$$R_s^{dust,i} = (M_d^i \kappa_v(B) / 2\pi \tau_B^f)^{1/2} \quad (8)$$

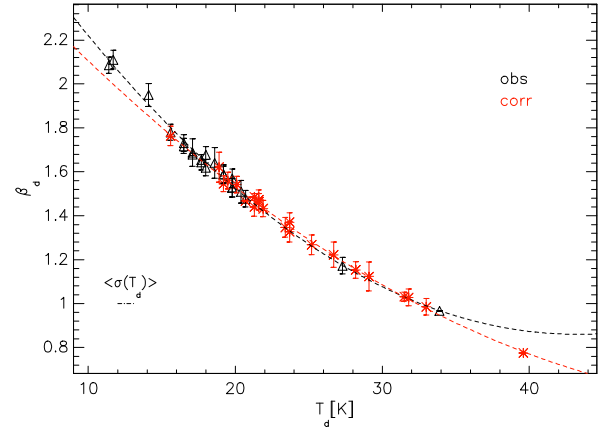


**Figure 1.** The dust temperature ( $T_d$ ) - dust emissivity index evolution ( $\beta_d$ ). The observed  $T_d$  are shown with black triangles, while the corrected ones are represented with red stars. The black (red) dotted curves are polynomial regression fits of second order to the observed (corrected) values. The error bars represent the standard deviations. The average standard deviation of  $T_d$  is overplotted in the lower left corner.

### 3.3 Error estimation

The uncertainties over  $d_{gal}$  (measured distance to the galaxy) were taken from the same references as before (see Table 1 in Paper I). The uncertainties of the  $250\mu m$  fluxes and metallicities were taken from the references where the respective values were found (Table 1), while the ones for  $M_d$ ,  $\tau_B$  and  $R_{s,d}(B)$  were already derived (also in Paper I). We then performed propagation of errors in Eqs. 3-8 to obtain the standard deviation ( $\sigma$ ) for all the needed parameters ( $T_d$ ,  $\beta_d$ ,  $R_s^{dust}$ ,  $\Sigma_d$ ), both the observed and intrinsic quantities. The values are also shown in Table 1.

## 4 RESULTS

We show here the main results of this study - an analysis of the relations between the dust temperature, its emissivity index,  $\beta$  (Sect. 4.1), and local / integrated ISM and SFR related quantities (Sect. 4.2-4.4). It is important to mention that all the plots show results for the whole sample considered - spirals and lenticulars. However, whenever necessary, we do underline the differences in the numerical results appearing when considering only the 19 spirals in our sample.

Throughout this section, some of the analysed relations are plotted in the linear form  $\log(Y) - \log(X)$ . The best-fit for each relation (from a linear regression procedure) has the general form  $\log(Y) = \beta + \alpha \times \log(X)$ , with  $\alpha$  - the intercept and  $\beta$  - the slope of the relation. Unless specified otherwise, all the intercepts and slopes are given in the same units as the ones of  $\log(Y)$  and  $\log(Y)/\log(X)$ .

### 4.1 The dust temperature - $\beta_d$ evolution

In Figure 1 we show the plotted variation of dust temperature with dust emissivity index. It can be observed the known anti-correlation between  $T_d$  and  $\beta_d$ , with its hyperbolic shape seen in many other studies. It is not yet clear if it has, at least in part, a physical origin (Shetty et al. 2009b; Smith et al. 2012; Galametz et al. 2012; Juvela et al. 2013; Rémy-Ruyer et al. 2013 or if it appears as a result of the  $\chi^2$  fitting technique (Shetty et al. 2009a). Other potential causes for this anti-correlation mentioned in the literature



are the noise in the NIR-FIR-submm data and temperature mixing along the line of sight (Shetty et al. 2009a,b; Juvela & Ysard 2012; Juvela et al. 2013; Tabatabaei et al. 2014), or the use of a single-temperature MBB - that does not account for a warm dust component to characterise the cold dust emission SED (Shetty et al. 2009a; Kelly et al. 2012; Juvela & Ysard 2012; Juvela et al. 2013), and can produce biased values for  $\beta_d$  (Kirkpatrick et al. 2014; Hunt et al. 2015; Bendo et al. 2023). We have fitted the data points with a second-order polynomial to better describe the hyperbolic trend. On a  $\log(T_d)$ - $\log(\beta_d)$  representation, the trend becomes linearly decreasing, and we get the best-fit relations for the observed and intrinsic values as

$$\log(\beta_d) = (-0.70 \pm 0.03)\log(T_d) + (1.09 \pm 0.04) \quad (9)$$

$$\log(\beta_d^i) = (-0.88 \pm 0.04)\log(T_d^i) + (1.32 \pm 0.03) \quad (10)$$

These relations are equivalent with  $\beta_d = 1.51(T_d/20)^{-0.70}$  and  $\beta_d = 1.55(T_d/20)^{-0.88}$ , for an easier comparison with other results in the literature, that give this relation in the form  $\beta_d = C(T_d/20)^\alpha$  (with  $C$  a constant). Compared with other studies, these values for the slope of the log-linear relation characterise a shallower relation. For example, Paradis et al. (2010) determined a relation  $\beta_d \propto T_d^{-1.33}$  for their analysed Herschel PACS and SPIRE maps, Smith et al. (2012) derived slopes of  $-1.57$  and  $-0.61$  for the outer and inner regions of their sample, Grossi et al. (2015) found a relation of  $\beta_d \propto T_d^{-1.55}$  for their sample of Virgo dwarf galaxies while Rémy-Ruyer et al. (2013) derived  $T_d \propto \beta_d^{-0.29}$  for the KINGFISH sample of spirals and S0s.

We have to underline here that despite using dust masses not derived from a SED fit but through another independent method, and without having to deal with the noise in all the observed NIR-FIR-submm fluxes (as unlike in other studies, we only use the  $250\mu\text{m}$  fluxes), we still observe the  $T_d - \beta_d$  degeneracy. So, while we have eliminated some of the causes for this degeneracy, it is still present, as we are still using a single-temperature MBB to characterise the dust emission overall in the galaxy. Likewise, by using an hierarchical Bayesian approach to fit the FIR SED, Lamperti et al. (2019) have only managed to reduce the degree of this anti-correlation and diminish the ranges of values for  $T_d$  and  $\beta_d$ , but not entirely eliminate it. Therefore, we have reasons to believe that this anti-correlation may still, at least in part, have a physical origin, and this cannot be completely avoided with the current methods used in SED fitting and dust temperature / dust mass calculation.

For the purpose of comparison with other similar relevant studies, it is important to mention here the mean values calculated for the dust temperature and emissivity index of the entire sample, in both cases. We actually derive these values for the spirals and S0s taken together (the whole sample), but also for the spiral galaxies only, for a more relevant comparison with other results. Thus, in the case when  $\beta_d$  was left free, we determined for the whole sample mean values of  $\langle T_d \rangle = 17.08 \pm 0.33\text{K}$  and  $\langle T_d^i \rangle = 22.40 \pm 0.81\text{K}$  for dust temperatures, and  $\langle \beta_d \rangle = 1.63 \pm 0.05$  and  $\langle \beta_d^i \rangle = 1.34 \pm 0.05$ . The mean dust temperature values are very consistent with values derived in Skibba et al. (2011); Galametz et al. (2012); Grootes et al. (2013); Rémy-Ruyer et al. (2013); Galametz et al. (2014); Grossi et al. (2015); Hunt et al. (2015). If we consider only the 19 spirals in the sample, then the values change, not dramatically though:  $\langle T_d \rangle = 15.44 \pm 0.26\text{K}$  and  $\langle T_d^i \rangle = 20.59 \pm 0.58\text{K}$ , while for dust emissivity index we obtain  $\langle \beta_d \rangle = 1.70 \pm 0.04$  and  $\langle \beta_d^i \rangle = 1.39 \pm 0.04$ . These values are also in very good agreement with the previously mentioned studies, where the methods were sometimes different. For the second case, with fixed  $\beta_d$ , the mean dust

temperatures for the whole sample are  $\langle T_d^{bfix} \rangle = 20.12 \pm 0.28\text{K}$ ,  $\langle T_d^{i,bfix} \rangle = 30.83 \pm 0.69\text{K}$ , while for the spiral galaxies only, we have  $\langle T_d^{bfix} \rangle = 17.05 \pm 0.23\text{K}$ ,  $\langle T_d^{i,bfix} \rangle = 26.59 \pm 0.50\text{K}$ . We can see right away that when  $\beta_d$  is constrained overall to a value higher than the one obtained in the  $\beta_d$ -free scenario, both the observed and corrected average dust temperatures of the whole sample, but also of the spirals sub-sample, are *systematically higher*.

All the numerical results for  $T_d, \beta_d$  and their standard deviations ( $\sigma$ ) can be found in Table 1.

#### 4.2 $T_d$ - ISM/SF local/integrated quantities scaling relations

In the following figure - Fig. 2, we plot the variation of dust temperature with metallicity (in the form of oxygen abundance,  $12+[O/H]$ ), with dust surface density ( $\Sigma_d$ ), but also with some of the star-formation related quantities, namely SFR and specific star-formation, sSFR. The later plots are produced to investigate if any of the SF quantities is a potential dust temperature tracer. As a means to compare the trends seen in the data and potential differences that may arise, we show on the upper row of Fig. 2 the plots for the case where  $\beta_d$  was left free, while the lower row of plots corresponds to the case with  $\beta_d = 2$ . In the first pair of plots, we see the metallicity (taken from Moustakas et al. 2010) variation with dust temperature. A slightly decreasing trend can be noticed when  $\beta_d$  is variable, for both the observed and corrected values, despite the large uncertainties for certain galaxies. A part of the spread in the data can be due to the use of the oxygen abundance as a tracer of the total metal mass in these galaxies. A similar result, though not very conclusive, was observed by Rémy-Ruyer et al. (2013) in their analysis of KINGFISH galaxies, while Cortese et al. (2014) obtained a correlation coefficient of  $-0.53$  for the same anti-correlation, in the case where they left  $\beta_d$  as a free parameter. For the second case, an inconclusive flat-like trend (as also noticed by Cortese et al. 2014 when fixing  $\beta_d$  to 2) can be seen, different from the first scenario. A basically flat trend was also found by Lamperti et al. (2019) for both their approaches - a single MBB and a Bayesian hierarchical SED fitting. The decreasing trend suggests that metal-rich galaxies have colder dust on average. This translates into important information about the dust grain composition and their properties.

On the second column in Fig. 2 we show the  $T_d$  vs dust surface density variation. A relation between these quantities would be expected if the population of young stars is the main contributor to the dust heating. A mild anti-correlation is noticeable when  $\beta_d$  is a free parameter, if we disregard some obvious outliers, with a slope  $\alpha = -1.27 \pm 0.87$  (corrected relation). A large scatter is present in both the observed and intrinsic values. This result means that colder dust is more concentrated in the disc of the galaxies and therefore has a more compact distribution. However this comes in opposition with the positive strong correlation found by Taylor et al. (2025) from their pixel-by-pixel analysis of a sample of spiral galaxies (a few also present in our sample), with correlation coefficients of 0.6 or higher. In the lower plot of the same column, we can see that when  $\beta_d = 2$ , the trend is reversed and we observe a mild increasing behaviour between  $T_d$  and  $\Sigma_d$ , with a slope of  $\alpha = 1.29 \pm 0.67$  for the corrected values.

In the third and fourth columns of the same figure, we show  $T_d$  variation with specific star-formation and the star-formation rate, SFR, for both cases. The trends in the plots are rather inconclusive, with a large scatter in the data. Fixing  $\beta_d$  does not produce more clear results. The same situation is for the  $T_d - \Sigma_{SFR}$  variation, which we do not show here. There is a weak increasing tendency between  $T_d$  and

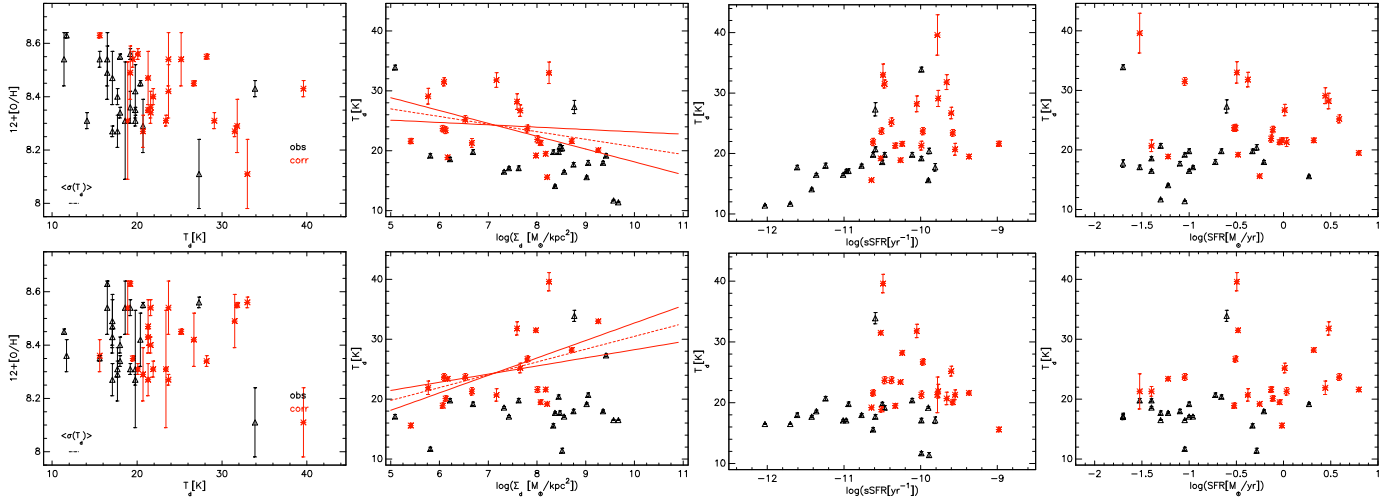


**Figure 2.** A comparison of the relations between the dust temperature ( $T_d$ ) and some of the relevant dust/ISM and star-formation related quantities, when  $\beta_d$  is either free or fixed to a value of 2.0. *Upper row:* Dust temperature vs. metallicity ( $Z[\text{O}/\text{H}]$ , taken from [Moustakas et al. 2010](#)), dust surface density ( $\Sigma_d$ ), sSFR and SFR, when  $\beta_d$  is left free; *Lower row:* the same plots for a fixed  $\beta_d = 2$  value. The red dotted line is a linear regression fit of the corrected values, while the two red solid ones delimit the  $\pm 1\sigma$  uncertainty range for the best-fit relation. The error bars represent the standard deviations. The average standard deviations of the abscissa quantities are overlapped on the figures.

sSFR, for the  $\beta_d$ -free case. A more clear increasing trend was observed for the relation between  $T_d$ , sSFR and  $\Sigma_{\text{SFR}}$  by [Chiang et al. \(2023\)](#), while [Lamperti et al. \(2019\)](#) found correlation coefficients of 0.54 and 0.49 for the  $T_d - \text{sSFR}$  and  $T_d - \Sigma_{\text{SFR}}$  relations. Our results suggest that sSFR, SFR,  $\Sigma_{\text{SFR}}$  are not conclusive tracers for the dust temperature. This result can be caused by either the low statistics of this study or the consideration of a single temperature MBB, which does not take into account a warmer dust component, present in the star-forming regions around the young stars.

While we do not show it here, we have to mention also that no increase or decrease of the dust-to-stellar mass ratio ( $M_d/M_*$ ) with  $T_d$  could be noticed, the trend being basically flat for both cases, with some scatter in the data.

#### 4.3 $\beta_d$ - ISM/SF local/integrated quantities scaling relations

In this section we explored some of the potential relations of  $\beta_d$  with relevant ISM and SF measurements. We show in Fig. 3 some of these relations. In the first panel, the variation of dust emissivity index is plotted against metallicity. A mild correlation can be observed, with slopes of  $0.23 \pm 0.10$  and  $0.22 \pm 0.11$  for the observed (corrected) relations, reduced level of scatter ( $\sigma = 0.21$  &  $0.17$  dex), while the derived corresponding Pearson correlation coefficients,  $r_{Z\beta_d}$ , have the values of 0.46 and 0.42. This relation has also been found in studies by [Boselli et al. \(2012\)](#); [Rémy-Ruyer et al. \(2013\)](#); [Cortese et al. \(2014\)](#); [Lamperti et al. \(2019\)](#), with correlation coefficients around 0.6 or higher (0.68 in [Cortese et al. 2014](#)). While the slope is quite shallow, this relation shows that metal-rich galaxies tend to have dust with a grain composition made predominantly from crystalline silicates, with less amorphous silicates present, as  $\beta_d$  is a parameter known to be in connection with grain physical properties. We should mention here that metallicity correlates even better with another property of dust, namely the dust mass. This relation, while not shown here, is a consequence of the fundamental mass-metallicity and  $M_d - M_*$  relations, and has a larger scatter and higher correlation coefficients than the  $Z - \beta_d$ , with  $\sigma = 0.70$ ,  $r_{M_d Z} = 0.50$  for the intrinsic relation.

In the second panel we show how  $\beta_d$  changes with the total stellar mass of the galaxy,  $M_*$ . Whereas in some works (e.g. [Cortese et al. 2014](#); [Lamperti et al. 2019](#)) a correlation between these two quantities - a local and an integrated one - has been observed (although with a rather shallow slope), here for our small sample the results are inconclusive. Thus, [Lamperti et al. \(2019\)](#) found a mid-strength correlation by analysing a sample of 192 galaxies from the JINGLE survey ([Saintonge et al. 2018](#)), but also found a relation for  $\beta_d - \mu_s$  and  $\beta_d - M_{\text{HI}}/M_\odot$  pairs ( $M_{\text{HI}}$  is the mass of neutral atomic hydrogen), while [Cortese et al. \(2014\)](#) found a weak ( $r = 0.49$ ) correlation for  $\beta_d - M_*$ , and stronger ones for the other two (with coefficients  $r=0.65$  and  $-0.70$  respectively), when  $\beta_d$  was left as a free parameter. We do not show here the other two plots as again, a clear conclusive trend was not identified and the data were quite scattered.

The third and fourth panels show the variation of dust emissivity index with the star-formation rate and specific SFR. Here a significant scatter in the data stands out in both plots, but nevertheless an increasing trend of SFR with  $\beta_d$  for the corrected values only could be noticed, while an anti-correlation for both the observed and corrected values can be seen in the last plot. For the last relation we obtained the best-fit parameters: slope  $\alpha = -1.10 \pm 0.66$ ,  $r_{\beta_d, \text{sSFR}} = -0.20$  - observed, and  $\alpha = -0.78 \pm 0.42$ ,  $r_{\beta_d, \text{sSFR}} = -0.76$ ,  $\sigma = 0.30$  dex - for the corrected data. We see that galaxies with higher star-formation rates, and therefore more active and with a higher dust production and dust mass ( $M_d$  correlates with SFR, [Grossi et al. 2015](#); [Pastrav 2024](#)) have also higher dust emissivity indices, and therefore more silicate rich grains. The slope of  $2.66 \pm 0.16$  and the increasing trend for  $\text{SFR} - \beta_d$  are not in agreement with the results of [Lamperti et al. \(2019\)](#) who did not observe a conclusive increase between these quantities or between  $\beta_d$  and sSFR. [Smith et al. \(2012\)](#) investigated the  $\text{SFR} - \beta_d$  relation but a clear correlation was not seen. In our case, given the large scatter in both the observed and corrected data points for the last two plots, for a more clear and definitive conclusion on the  $\text{SFR} - \beta_d$  and  $\text{sSFR} - \beta_d$ , a larger sample would be beneficial.

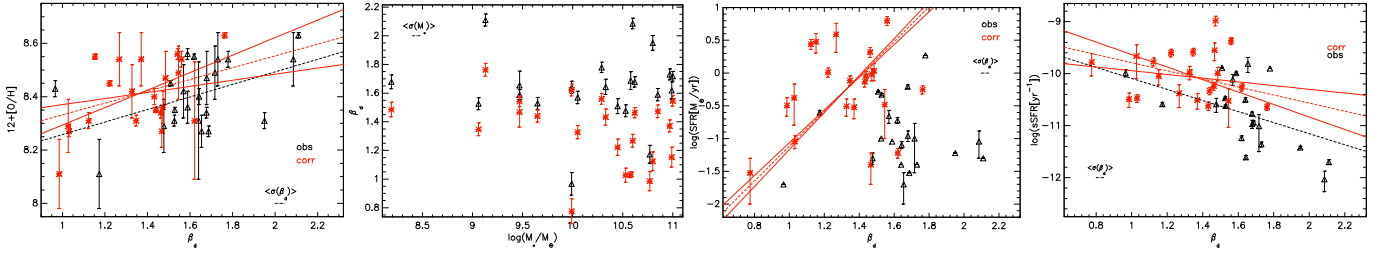


**Figure 3.** The relation between the dust emissivity index,  $\beta_d$ , and other ISM/SFR quantities: metallicity ( $12+[O/H]$ ), stellar mass ( $M_\odot$ ), SFR and sSFR. The black dotted line is a linear regression fit of the observed values. The two red solid lines delimit the  $\pm 1\sigma$  uncertainty range for the best-fit relation of the corrected values. The rest of symbols, colors and lines have the same meaning as those in Fig. 2.

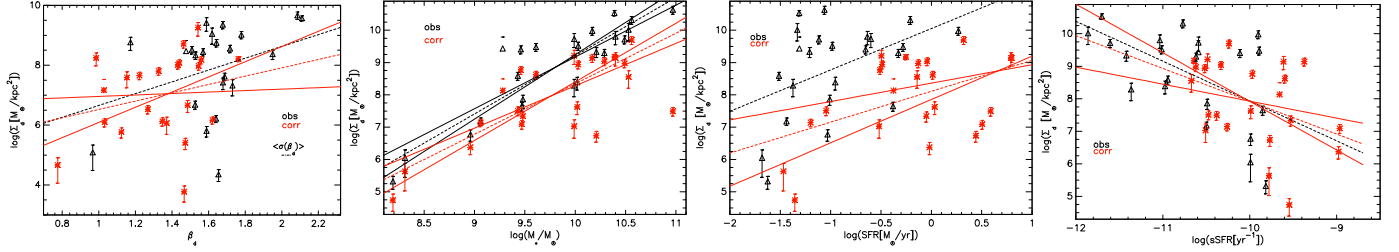


**Figure 4.** The relation between the dust surface density,  $\Sigma_d$  and other dust/ISM/SFR quantities:  $\beta_d$ , stellar mass ( $M_\odot$ ), SFR and sSFR. The black dotted line is a linear regression fit of the observed values, while the two black solid lines delimit the  $\pm 1\sigma$  uncertainty range for the best-fit relation of the observed values. The rest of symbols, colors and lines have the same meaning as those in Fig. 2.

#### 4.4 $\Sigma_d$ - ISM/SF local/integrated quantities scaling relations

In this section, we investigated the relations between the dust surface density and some of the relevant dust, ISM and SF parameters - namely  $\beta_d$ ,  $M_*$ ,  $SFR$ , and  $sSFR$ . From the following Fig. 4, one can see that the strongest correlation and lowest scatter ( $\sigma$ ) for the dust surface density is with the stellar mass (second panel). For this relation we derived correlation coefficients  $r_{\Sigma_d, M_*}$  of 0.89 and 0.81 for the observed and corrected values, which underlines the strength of this correlation. The corresponding slope and scatter for the corrected data points are  $\alpha = 1.56 \pm 0.25$  and  $\sigma = 0.63\text{dex}$ , respectively, with a slightly higher slope and comparable  $\sigma$  for the measured values.

As  $\Sigma_d \propto M_d$  (Eq. 6), this relation can be considered a consequence / result of the more tight  $M_d - M_*$  relation (Grootes et al. 2013; De Vis et al. 2017; van der Giessen et al. 2022; Pastrav 2024). To further investigate this issue, we did a linear partial correlation analysis for the  $(\Sigma_d, M_*, M_d)$  quantities, deriving the corresponding partial correlation coefficients:  $r_{M_* \Sigma_d, M_d} = -0.105$ ,  $r_{\Sigma_d M_d, M_*} = 0.673$  and  $r_{M_* M_d, \Sigma_d} = 0.747$ . These values suggest that  $M_d$  is a more important quantity than  $\Sigma_d$  for the stellar mass  $M_*$ . This was somehow expected as the  $M_d - M_*$  correlation was found to be very strong and tight ( $r_{M_d, M_*} = 0.92$  for the corrected values, low scatter  $\sigma$ ). However, as our sample is small, better statistics would certainly strengthen this conclusion.

In the first panel of the same figure we verified if there exists a relation between  $\Sigma_d$  and  $\beta_d$ . We assumed there should be, as both of these quantities are dust-related, even though one characterises an intrinsic property of the dust grains ( $\beta_d$ ) while the other is a measure of the distribution of dust within the associated disc ( $\Sigma_d$ ). This could be investigated here as we considered  $\beta_d$  as a free parameter, but not in other studies where it was fixed. One can see the large scatter in both the observed and corrected data values. The derived correlation coefficients indicate a rather moderate correlation for the spirals, as  $r_{\Sigma_d, \beta_d} = 0.43$  for the observed values, and 0.42 for the intrinsic ones.

This relation is, at least according to our knowledge, *new*, as it was not been observed in other studies. It shows that dust grains with a higher composition of silicates can be found in galaxies with a more compact dust distribution, where processes of dust growth (through coagulation and material accretion) may be more prevalent, given the increased shielding from the incoming radiation.

In the third panel, we plotted  $\Sigma_d$  as a function of the star-formation rate. A relation between these two parameters would be expected given the  $\tau - SFR$  correlation found in Paper III (see there Fig. 6), the proportionality relation between  $\tau$  and  $\Sigma_d$  ( $\tau = \kappa_r \Sigma_d$ ) and also because new stars are born in birthclouds of dust and gas. There is a large scatter in the data points (as in the case of the  $\tau - SFR$  relation) and a mild increase in the dust surface density with SFR, with a rather shallow slope of  $0.95 \pm 0.38$  for the corrected values. The derived Pearson coefficients are quite low - 0.45 & 0.47, which also shows the mild strength of this relation. A strong correlation was also observed in Smith et al. (2012), for the outer regions of their analysed galaxies. In comparison, the trend of  $\Sigma_d$  with the specific star-formation rate is considerably stronger, as it can be noticed in the last panel of Fig. 4. The characteristic parameters of this relation are:  $\alpha = -1.01 \pm 0.48$  and  $-1.22 \pm 0.36$  for the slopes (corrected / observed),  $r_{\Sigma_d, sSFR} = -0.42$  and  $-0.59$  for the corresponding correlation coefficients. The spread of the data points is still quite significant for this relation too. This last relation shows that dust is more compactly distributed in galaxies with lower sSFR, and therefore higher stellar mass and higher dust attenuation (given the known anti-correlation  $sSFR - M_*$  and the  $M_d - M_*$  correlation).

While we do not show it here, we note that  $\Sigma_d$  and the stellar mass surface density ( $\mu_*$ ) are not correlated.

**Table 1.** Dust temperature and dust emissivity index for the whole sample. The different columns represent: (1) - galaxy name; (2) - integrated flux at  $250\mu\text{m}$  taken from: *a* - Aniano et al. (2020), *b* - Dale et al. (2017); *c* - O’Halloran et al. (2010); (3) - dust temperature (free  $\beta_d$ ); (4) - intrinsic (corrected) dust temperature (free  $\beta_d$ ); (5) - dust emissivity index; (6) - intrinsic (corrected) dust emissivity index; (7) - dust temperature (fixed  $\beta_d$ ); (8) - corrected dust temperature (fixed  $\beta_d$ ); (9) - observed dust surface density; (10) - intrinsic (corrected) dust surface density; (11) - gas-phase metallicity (oxygen abundances), taken from: Moustakas et al. (2010). In square brackets we have the units in which these quantities are given.

<i>Galaxy</i>	$f_{250}$	$T_d$	$T_d^i$	$\beta_d$	$\beta_d^i$	$T_d$	$T_d^i$	$\Sigma_d$	$\Sigma_d^i$	$12 + [O/H]$
	[Jy]	[K]	[K]			[K]	[K]	[ $\frac{M_\odot}{\text{kpc}^2}$ ]	[ $\frac{M_\odot}{\text{kpc}^2}$ ]	
(1)	(2)	(3)	(4)	(5)	(6)	(7)	(8)	(9)	(10)	(11)
NGC 0628	$61.00 \pm 4.70^a$	$19.80 \pm 0.34$	$21.30 \pm 0.42$	$1.53 \pm 0.04$	$1.44 \pm 0.04$	$5.60 \pm 0.29$	$19.50 \pm 0.29$	$8.33 \pm 7.78$	$8.07 \pm 7.52$	$8.35 \pm 0.01$
NGC 2841	$33.90 \pm 2.50^a$	$15.60 \pm 0.16$	$19.50 \pm 0.30$	$1.78 \pm 0.04$	$1.56 \pm 0.04$	$19.20 \pm 0.15$	$21.60 \pm 0.15$	$9.02 \pm 8.46$	$8.18 \pm 7.62$	$8.54 \pm 0.03$
NGC 2976	$24.60 \pm 1.80^a$	$19.20 \pm 0.32$	$21.60 \pm 0.44$	$1.59 \pm 0.04$	$1.47 \pm 0.04$	$11.70 \pm 0.27$	$15.60 \pm 0.27$	$5.81 \pm 5.39$	$5.41 \pm 5.02$	$8.36 \pm 0.06$
NGC 3031	$176.00 \pm 13.00^b$	$11.70 \pm 0.08$	$15.60 \pm 0.20$	$2.11 \pm 0.04$	$1.76 \pm 0.04$	$16.50 \pm 0.09$	$19.20 \pm 0.09$	$9.57 \pm 8.86$	$8.21 \pm 7.50$	$8.63 \pm 0.01$
NGC 3190	$8.50 \pm 0.58^a$	$16.50 \pm 0.18$	$19.20 \pm 0.27$	$1.72 \pm 0.03$	$1.55 \pm 0.04$	$17.10 \pm 0.16$	$31.50 \pm 0.16$	$8.56 \pm 8.00$	$7.98 \pm 7.42$	$8.49 \pm 0.10$
NGC 3621	$37.00 \pm 4.60^a$	$17.10 \pm 0.35$	$31.50 \pm 0.67$	$1.69 \pm 0.06$	$1.03 \pm 0.02$	$19.80 \pm 0.31$	$23.70 \pm 0.31$	$7.62 \pm 7.07$	$6.09 \pm 5.58$	$8.27 \pm 0.02$
NGC 3938	$22.90 \pm 1.90^a$	$19.80 \pm 0.34$	$23.70 \pm 0.60$	$1.57 \pm 0.04$	$1.33 \pm 0.05$	$20.40 \pm 0.30$	$26.70 \pm 0.30$	$8.44 \pm 7.89$	$7.80 \pm 7.25$	$8.42 \pm 0.10$
NGC 4254	$62.00 \pm 6.00^a$	$20.40 \pm 0.46$	$26.70 \pm 0.95$	$1.51 \pm 0.05$	$1.22 \pm 0.06$	$11.40 \pm 0.39$	$25.20 \pm 0.39$	$8.52 \pm 7.96$	$7.66 \pm 7.10$	$8.45 \pm 0.01$
NGC 4594	$23.50 \pm 1.60^a$	$11.40 \pm 0.07$	$25.20 \pm 0.66$	$2.09 \pm 0.04$	$1.27 \pm 0.05$	$16.50 \pm 0.08$	$23.70 \pm 0.08$	$9.67 \pm 9.11$	$6.53 \pm 6.02$	$8.54 \pm 0.10$
NGC 4736	$65.00 \pm 7.00^a$	$14.10 \pm 0.17$	$29.10 \pm 1.33$	$1.95 \pm 0.05$	$1.12 \pm 0.07$	$17.70 \pm 0.16$	$21.90 \pm 0.16$	$8.37 \pm 7.90$	$5.77 \pm 5.34$	$8.31 \pm 0.03$
NGC 4826	$42.40 \pm 3.00^a$	$16.50 \pm 0.19$	$23.70 \pm 0.53$	$1.73 \pm 0.04$	$1.37 \pm 0.04$	$18.60 \pm 0.17$	$18.90 \pm 0.17$	$7.32 \pm 7.07$	$6.06 \pm 5.83$	$8.54 \pm 0.10$
NGC 5055	$138.00 \pm 9.00^a$	$17.70 \pm 0.33$	$21.90 \pm 0.59$	$1.64 \pm 0.05$	$1.43 \pm 0.06$	$18.00 \pm 0.29$	$21.60 \pm 0.29$	$8.75 \pm 8.19$	$8.01 \pm 7.45$	$8.40 \pm 0.03$
NGC 5474	$9.13 \pm 0.43^a$	$18.60 \pm 0.29$	$18.90 \pm 0.30$	$1.64 \pm 0.04$	$1.62 \pm 0.04$	$19.80 \pm 0.25$	$23.40 \pm 0.25$	$6.22 \pm 5.64$	$6.17 \pm 5.59$	$8.31 \pm 0.22$
NGC 7331	$88.20 \pm 6.20^a$	$18.00 \pm 0.22$	$21.60 \pm 0.36$	$1.68 \pm 0.04$	$1.46 \pm 0.04$	$18.00 \pm 0.20$	$28.20 \pm 0.20$	$9.35 \pm 8.79$	$8.71 \pm 8.15$	$8.34 \pm 0.02$
NGC 7793	$54.00 \pm 3.70^a$	$19.80 \pm 0.35$	$23.40 \pm 0.55$	$1.53 \pm 0.04$	$1.35 \pm 0.04$	$19.20 \pm 0.30$	$20.10 \pm 0.30$	$6.69 \pm 6.17$	$6.13 \pm 5.61$	$8.31 \pm 0.02$
NGC 5194	$203.00 \pm 14.00^b$	$18.00 \pm 0.38$	$28.20 \pm 1.31$	$1.62 \pm 0.06$	$1.15 \pm 0.07$	$20.70 \pm 0.33$	$31.80 \pm 0.33$	$9.05 \pm 8.79$	$7.59 \pm 7.33$	$8.55 \pm 0.01$
NGC 5033	$40.78 \pm 2.85^a$	$19.20 \pm 0.27$	$20.10 \pm 0.31$	$1.59 \pm 0.04$	$1.54 \pm 0.04$	$27.30 \pm 0.23$	$33.00 \pm 0.23$	$9.42 \pm 9.10$	$9.26 \pm 8.94$	$8.56 \pm 0.02$
NGC 1377	$1.22 \pm 0.08^a$	$20.70 \pm 0.38$	$31.80 \pm 1.22$	$1.48 \pm 0.04$	$1.03 \pm 0.05$	$17.70 \pm 0.32$	$20.70 \pm 0.32$	$8.47 \pm 8.57$	$7.17 \pm 7.27$	$8.29 \pm 0.10$
NGC 1482	$15.40 \pm 1.00^a$	$27.30 \pm 1.10$	$33.00 \pm 1.79$	$1.17 \pm 0.06$	$0.99 \pm 0.07$	$33.90 \pm 0.92$	$39.60 \pm 0.92$	$8.77 \pm 8.43$	$8.25 \pm 7.91$	$8.11 \pm 0.13$
NGC 1705	$0.85 \pm 0.13^c$	$17.70 \pm 0.61$	$20.70 \pm 0.97$	$1.65 \pm 0.10$	$1.47 \pm 0.10$	$17.10 \pm 0.53$	$21.30 \pm 0.53$	$4.36 \pm 3.99$	$3.78 \pm 3.52$	$8.27 \pm 0.06$
NGC 3773	$0.94 \pm 0.07^a$	$33.90 \pm 0.38$	$39.60 \pm 3.34$	$0.97 \pm 0.08$	$0.78 \pm 0.09$	$17.10 \pm 0.32$	$21.30 \pm 0.32$	$5.09 \pm 4.96$	$4.67 \pm 4.54$	$8.43 \pm 0.03$
NGC 5866	$7.57 \pm 0.53^a$	$17.10 \pm 0.21$	$21.30 \pm 0.73$	$1.68 \pm 0.05$	$1.49 \pm 0.05$	$17.10 \pm 0.18$	$21.30 \pm 0.18$	$7.42 \pm 7.06$	$6.66 \pm 6.30$	$8.47 \pm 0.10$

#### 4.5 The dust spatial distribution vs. optical stellar continuum emission extents

We investigated here how does the dust spatial distribution compares with the optical continuum, corresponding to the stellar emission. We have already seen in Paper III that the star-formation disc is slightly more extended than the stellar emission one (see Fig. 8). As both components are considered to have an exponential disc type of distribution, we compared the scale-lengths of the dust and stellar discs. We plotted their ratio,  $R_s^{\text{dust}}/R_{s,d}(B)$ , as a function of the stellar mass, in the upper panel of Fig. 5, for the observed (black) and corrected values (red). The B band stellar disc scale-lengths,  $R_{s,d}(B)$  were determined in Paper I. One can see that on average, the dust disc scale-lengths are slightly smaller than the optical stellar disc ones, and their is a very mild increase of their ratio with  $M_*$ . We derived the average observed ratios of  $0.84 \pm 0.15/0.94 \pm 0.14$  (with / without outliers), and  $0.78 \pm 0.16/0.80 \pm 0.15$  respectively (with / without outliers), for the intrinsic ones. We can see that for some cases the ratios are up to 1.5 and beyond, which means that the exponential dust discs are considerably more extended than their stellar ones. Muñoz-Mateos et al. (2009) fitted the dust surface density profiles of SINGS galaxies with an exponential function and found an average factor of 1.1 between the derived dust disc scale-lengths and the stellar emission ones derived from data at  $3.6\mu\text{m}$ . Casasola et al. (2017) determined likewise an average ratio of 1.1 for the scale-lengths at  $250\mu\text{m}$  and  $3.6\mu\text{m}$ , while Hunt et al. (2015), by analysing the whole KINGFISH sample through exponential fits of the radial profiles at the same  $3.6\mu\text{m}$  and  $250\mu\text{m}$  wavelengths, determined a mean value of  $0.96 \pm 0.36$  for the ratio of exponential scale-lengths of the cool dust and stars distributions. Therefore, our results are in agreement (within errors) with these studies, although

a direct comparison is not possible due to different wavelengths considered within each study. Nevertheless, our ratios (which consider the B band stellar emission scale -lengths) can be more relevant in this context, since dust emission is connected in a higher proportion to the young stellar population.

We also plotted in the lower panel of the same figure the two scale-lengths against each other. A linear monotonic increase can be noticed, which means that galaxies with a larger extent of the stellar disc also have a larger extent of the dust disc. We determined a slope of  $\alpha = 0.59 \pm 0.09$  for the intrinsic (dust-corrected) ratios, consistent within errors with the value of 0.69 found by Qin et al. (2024) (from their model) but slightly lower than the ones found by Mosenkov et al. (2022) -  $0.81 \pm 0.31$ , for the scalelengths at 100 and  $3.4\mu\text{m}$ , and Casasola et al. (2017), who found  $0.83 \pm 0.05$  for the pair of scale-lengths at 100 and  $3.6\mu\text{m}$ . The derived correlation coefficient  $r_{R_d^{\text{dust}}, R_{s,d}(B)} = 0.55$  is close to the value of 0.60 derived in Mosenkov et al. (2022) for their scale-lengths. Of course, as already mentioned here, we need to remember that the ratio of dust and stellar disc scale-lengths depends on the wavelengths, but also on the redshift (if we consider the inside-out galaxy evolution scenario the stellar disc extent will increase as the redshift decreases, whereas the precise evolution of the dust disc size is more complicated to predict), and so a direct and meaningful comparison with the previously mentioned studies (and others), is not straightforward. Moreover, the stellar disc scale-length is affected mainly by dust effects, and to a lesser extent by projection and decomposition effects (Pastrav et al. 2013a,b). Therefore, a more meaningful comparison would be between the intrinsic (dust-corrected) ratios - the red values, and similar intrinsic ratios from other studies, where available.



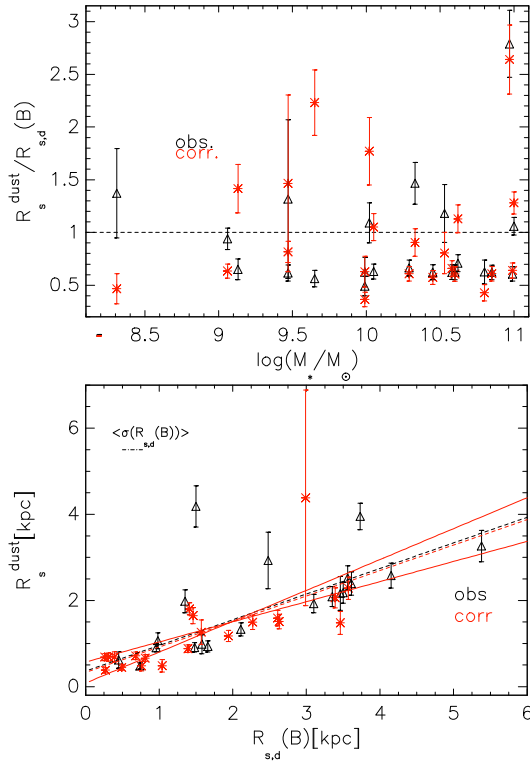


**Figure 5.** *Upper panel* The ratio between the observed (black triangles) / intrinsic (red stars) scale-lengths of the dust discs and the ones of the stellar emission discs (seen in optical B band), as a function of the stellar mass. *Lower panel* The same scale-lengths, plotted against each other. The black and red dotted line show a linear-regression best-fit of the observed and corrected values. The rest of symbols, colors and lines have the same meaning as those in Fig. 2.

## 5 DISCUSSION

In this section we are coming back to a few issues noticed when analysing the main results, evaluate the potential sources of systematic errors and other uncertainties, and discuss the limitations of the method.

### 5.1 Potential sources of systematic errors

The most important source of systematic errors in this study is the consideration of a single-temperature MBB function to characterise the cold dust emission in the NIR-submm range, that does not take into account a warmer dust component. The end result is a mean dust temperature. However, this approach has been largely used in the literature, producing noteworthy results. One way to ameliorate this is the consideration of two modified blackbody functions to characterise the cold and warm dust emission (each component with its own temperature and  $\beta_d$ ) or a broken MBB (BMBB, with a broken emissivity law; Gordon et al. 2014) - which allows for a variation in the wavelength dependence of the dust emissivity law (therefore having two  $\beta_d$  values for shorter and longer wavelengths, and a break wavelength as a parameter), to account for a sub-mm excess. These approaches have been attempted in Lamperti et al. (2019) on a sample of 192 low-redshift galaxies and revealed very small changes in the determined dust masses between each of these three situations. The dust temperatures derived for the BMBB are slightly lower than for the single MBB case, while  $\beta_d$  of the cold dust component is

slightly larger. In the case of two MBB, the authors found a smaller  $T_d$  than for the single MBB case, with dust emissivity indices similar for both. Having already the dust masses previously determined (a single set of measurements, for the cold dust component), it is not straightforward to check these two scenarios for our sample, particularly the one with two MBB (in which case we would need two sets of dust masses derived apriori, for the cold and warm components). In another study, using their analytical model to create dust SEDs and testing it on high-redshift galaxies, Somovigo & Algera (2025) found that considering multi-temperature dust can determine significantly underestimated dust masses and systematically flatter  $\beta_d$  values.

Related to the systematic errors caused by using a single-temperature MBB is the consideration of the cold dust SED peak at a fixed  $\lambda_{\text{peak}} = 250\mu\text{m}$  for the whole sample. Despite the fact that all galaxies analysed here are at very low-redshifts, some differences may exist in the values of  $\lambda_{\text{peak}}$  between galaxies which can introduce a systematic bias. However, we appreciate this bias to be within the error limits of the derived dust temperatures and emissivity indices.

Another way to improve this approach and better constrain  $\beta_d$  would be to consider the Rayleigh-Jeans side of the SED (fluxes in the sub-mm range) and use the slope of this part of the SED to derive this parameter (e.g. Bendo et al. 2024). This would of course require observational data in that wavelength range, that could be available from surveys such as ALMA or the proposed Atacama Large Aperture Submillimeter Telescope (AtLAST, Liu et al. 2025).

Another source of uncertainty would be the consideration of a fixed  $\kappa_{v_0}$  characteristic for a dust model with a fixed value for  $\beta_d$ , as the dust mass absorption coefficient is not very well constrained and it is not certain how it varies with radius. However, we have shown in Sect. 3.1 that this effect is cancelled here and this should not bias the derived  $(T_d, \beta_d)$  values. As we have used dust masses derived separately from this study, to determine dust temperatures and emissivity indices, a systematic bias (that cannot be overcome at this point) can be introduced by the choice of the Draine (2003) dust model, its characteristics being encapsulated in the  $K(B)$  constant.

Connected with this is the fact that we considered  $\kappa_{v_0}$  at a reference wavelength  $\lambda_0 = 100\mu\text{m}$ . As in other studies various reference wavelengths were used (e.g.  $250\mu\text{m}$ ,  $350\mu\text{m}$ ,  $850\mu\text{m}$  or others), a systematic bias can be introduced by this choice. But that would be true even with a different choice of  $\lambda_0$ , and of course some small differences may arise in the best-fit values of  $(T_d, \beta_d)$  as a result of this. However, the variation of  $(T_d, \beta_d)$  with  $\lambda_0$  is beyond the scope of this paper.

### 5.2 Limitations of the method and range of applicability

The limitations of the proposed method to derive  $(T_d, \beta_d)$  values and its range of applicability are tightly connected to the range of applicability of the relations used to determine the dust masses (and dust optical depths needed for  $M_d$ ) in Paper I - Eqs. 1&2. These in turn depend on the range of applicability of the fixed large-scale dust-star geometry (dust and stars distributed in exponential discs) as calibrated in the Popescu et al. (2011) model to the range of galaxy types, morphologies (same as for the dust and inclination effects numerical corrections) and stellar mass surface densities,  $8.0 \leq \log(\mu_*) \leq 11.0$  (therefore intermediate mass galaxies), one has to analyse with this method.

Another limitation would be the lack of a  $250\mu\text{m}$  flux/luminosity for certain galaxies. However, one can use in that case the  $160\mu\text{m}$  flux or luminosity (if available), especially for higher redshift galaxies. We

tested this for our nearby galaxies to check if / how the results would change in this case. We noticed that differences arise in the  $T_d$  and  $\beta_d$  values, but the trends seen in the analysed relations are conserved, with some small differences in their characteristic parameters.

## 6 SUMMARY AND CONCLUSIONS

In this paper we have presented a simple method to derive dust temperatures and dust emissivity indices, based on previous results - the dust masses derived (independent of this study) in Paper I and previous prescriptions. For consistency, and as a case study for validation of the method, we have used the sample of spiral and lenticular galaxies from the KINGFISH survey, for which we have determined the dust masses and other quantities.

A modified blackbody function was considered to characterise the cold dust emission SED in the NIR-submm wavelength range, while only the flux / luminosity at  $250\mu\text{m}$ , characteristic for the peak of the cold dust emission, was required for the presented approach. Thus, a time consuming whole SED fit was not necessary. We derived dust temperatures and corresponding dust emissivity indices for the same galaxies analysed in Papers I and III, through a grid-type procedure. Two scenarios were considered - one where  $\beta_d$  was left free, and another where  $\beta_d$  was fixed to a value commonly used in other works,  $\beta_d = 2$ . We then quantified the  $T_d - \beta_d$  evolution (and its potential degeneracy), and investigated new or confirmed relations between  $\Sigma_d, \beta_d$ , metallicity, SFR, and their implications for ISM evolution and star-formation.

Our main results are as follows:

- the hyperbolic shape of the  $T_d - \beta_d$  anti-correlation is again found, despite using dust masses that are not an output of a full cold dust SED fit but are derived through another independent method, and without the noise associated with all the observed NIR-FIR-submm fluxes; this fact suggests that this anti-correlation may have, at least partially, a physical origin;
- the means for observed and intrinsic  $T_d$  and  $\beta_d$  (when  $\beta_d$  is left free) and their range of values are consistent with many other similar studies; when  $\beta_d = 2$ , both the observed and corrected average dust temperatures are *systematically higher*;
- the mild anti-correlations in  $T_d - 12 + [O/H]$  and  $T_d - \Sigma_d$  show that metal-rich galaxies have colder dust on average, while colder dust is more concentrated in the disc of the galaxies, if  $\beta_d$  is left free; when  $\beta_d = 2$ , the opposite happens for the latter relation;
- SFR, sSFR and  $\Sigma_{SFR}$  are not conclusive tracers of dust temperature, in both scenarios;
- metal-rich galaxies tend to have dust with higher SFR and  $\beta_d$ , and therefore a grain composition made predominantly from crystalline silicates;
- $\Sigma_d$  correlates strongest with  $M_*$ , but this is a consequence of the fundamental  $M_d - M_*$  relation; *new, mild correlation*  $\Sigma_d - \beta_d$  is observed;
- dust is more compactly distributed in galaxies with lower sSFR, and therefore higher stellar mass and higher dust attenuation;
- a linear monotonic increase of the sizes of stellar discs with the dust disc ones is noticed, with a slope  $\alpha = 0.59 \pm 0.09$ , consistent with other results;
- on average, the dust disc scale-lengths are comparable with the scale-lengths of the optical stellar discs, slightly smaller, with some cases where these are considerably higher.

While this was a case study, where we have used a well studied small sample of representative galaxies in the nearby Universe, the same

simple procedure can be applied to other suitable, larger samples of low to mid-redshift normal galaxies, using the suite of prescriptions presented in Paper I (needed for dust opacity and dust mass calculation), III (for SFR and related parameters) and in this paper (to derive dust temperature and dust emissivity index), for larger scale studies of star-formation and ISM evolution.

## ACKNOWLEDGEMENTS

This research made use of the NASA/IPAC Extragalactic Database (NED), which is operated by the Jet Propulsion Laboratory, California Institute of Technology, under contract with the National Aeronautics and Space Administration.

This research was supported by the Romanian Ministry of Research, Innovation and Digitalization under the Romanian National Core Program LAPLAS VII - contract no. 30N/2023

## DATA AVAILABILITY

The data underlying this article are available in the article.

## REFERENCES

- Algera H. S. B., Inami, H., De Looze, I. et al. 2024, MNRAS, 533, 3098  
 Aniano, G., Draine, B. T., Hunt, L. K. et al. 2020, ApJ, 889, 150  
 Bendo, G. J., Baes, M., Bianchi, S. et al. 2014, MNRAS, 448, 135  
 Bendo G. J., Urquhart, S. A., Serjeant, S. et al. 2023, MNRAS, 522, 2995  
 Bendo, G. J., Bakx, T. J. L. C., Algera, H. S. B. et al. 2024, MNRAS, 540, 1560  
 Bianchi, S. 2013, A&A, 552, A89  
 Bianchi, S., De Vis, P., Viaene, S. et al. 2018, A&A, 620, A112  
 Boselli, A., Ciesla, L., Cortese, L., et al. 2012, A&A, 540, A54  
 Casasola, V., Cassarà, L. P., Bianchi, S. et al. 2017, A&A, 605, A18  
 Chiang, I.-Da, Hirashita, H., Chastenet, J. et al. 2023, MNRAS, 520, 5506  
 Clemens, M. J., Negrello, M., De Zotti, G. et al. 2013, MNRAS, 433, 695  
 Cortese, L., Fritz, J., Bianchi, S. et al. 2014, MNRAS, 440, 942  
 Dale, D. A., Aniano, G., Engelbracht, C. W., et al. 2012, ApJ, 745, 95  
 Dale, D. A., Cook, D. O., Roussel, H. et al. 2017, ApJ, 837, 90  
 De Looze, I., Lamperti, I., Saintonge, A. et al. 2020, MNRAS, 496, 3668  
 De Vis, P., Dunne, L., Maddox, S., et al. 2017, MNRAS, 464, 4680  
 Draine B. T., Lee H. M., 1984, ApJ, 285, 89  
 Draine, B.T. 2003, ARAA, 41, 241  
 Draine, B. T. & Li, A. 2007, ApJ, 657, 810  
 Driver, S. P., Popescu, C. C., Tuffs, R. J. et al. 2007, MNRAS, 379, 1022  
 Dunne, L., Eales, S.A., Edmunds, M. et al. 2000, MNRAS, 315, 115  
 Dunne, L. & Eales, S.A. 2001, MNRAS, 327, 697  
 Eales, S.A. & Edmunds, M.G. 1996, MNRAS, 280, 1167  
 Galametz, M., Kennicutt, R., Albrecht, M. et al. 2012, MNRAS, 425, 763  
 Galametz, M., Albrecht, M., Kennicutt, R. et al. 2014, MNRAS, 439, 2542  
 Galliano, F., Galametz, M., & Jones, A. P. 2018, ARA&A, 56, 673  
 Gordon K. D., Roman-Duval, J., Bot, C. et al. 2014, ApJ, 797, 85  
 Grootes, M., Tuffs, R.J., Popescu, C.C. et al. 2013, ApJ, 766, 59  
 Grossi, M., Hunt, L. K., Madden, S. C. et al. 2015, A&A, 574, A126  
 Hunt L. K. et al., 2015, A&A, 576, A33  
 Juvela, M., Ristorcelli, I., Pelkonen, V.-M. et al. 2011, A&A, 527, A111  
 Juvela, M. & Ysard, N. 2012, A&A, 541, A33  
 Juvela, M., Montillaud, J., Ysard, N., & Lunttila T. 2013, A&A, 556, A63  
 Juvela, M. 2022, A&A, 673, A145  
 Kelly, B. C., Shetty, R., Stutz, A. M. et al. 2012, ApJ, 752, 55  
 Kennicutt, R. C. J. 1998, ARA&A, 36, 189  
 Kennicutt, R. C., Armus, L., Bendo, G. et al. 2003, PASP, 115, 928

- Kennicutt, R. C., Lee, J. C., Funes, J. G., Sakai, S. & Akiyama, S. 2008, *ApJ*, 178, 247
- Kennicutt, R. C., Hao, C.-N., Calzetti, D., Moustakas, J., Dale, D. A. et al. 2009, *ApJ*, 703, 1672
- Kennicutt, R. C., Calzetti, D., Aniano, G. et al. 2011, *PASP*, 123, 1347
- Kirkpatrick, A., Calzetti, D., Kennicutt, R., et al. 2014, *ApJ*, 789, 130
- Kreckel, K., Groves, B., Schinnerer, E. et al. 2013, *ApJ*, 771, 62
- Kreckel, K., Groves, B., Bigiel, F. et al. 2017, *ApJ*, 834, 174
- Lamperti, I., Saintonge, A., De Looze, I. et al. 2019, *MNRAS*, 489, 4389
- Li, A., & Draine, B. T. 2001, *ApJ*, 554, 778
- Liu D, Saintonge A, Bot C et al. [version 2; peer review: 2 approved, 1 approved with reservations], *Open Res Europe* 2025, 4:148 (<https://doi.org/10.12688/openreseurope.17459.2>)
- Mosenkov, A., Usachev, P. A., Shakespear, Z. et al. 2022, *MNRAS*, 515, 5698
- Moustakas, J., Kennicutt, Jr., R. C., & Tremonti, C. A. 2006, *ApJ*, 642, 775
- Moustakas, J., Kennicutt, Jr., R. C., Tremonti, C. A. et al. 2010, *ApJS*, 190, 233
- Muñoz-Mateos, J. C., Gil de Paz, A., Boissier, S. et al. 2009, *ApJ*, 701, 1965
- O’Halloran, B., Galametz, M., Madden, S. et al. 2010, *A&A*, 518, L58
- Paradis D., Veneziani, M., Noriega-Crespo, A. et al. 2010, *A&A*, 520, L8
- Pastrav, B. A., Popescu, C. C., Tuffs, R. J., Sansom, A. E., 2013a, *A&A*, 553, A80
- Pastrav, B. A., Popescu, C. C., Tuffs, R. J., Sansom, A. E. 2013b, *A&A*, 557, A137
- Pastrav, B. A. 2020, *MNRAS*, 493, 3580
- Pastrav, B. A. 2021, *MNRAS*, 506, 452
- Pastrav, B. A. 2024, *MNRAS*, 527, 11167
- Planck Collaboration XIV, 2014, *A&A*, 564, A45
- Planck Collaboration XXII, 2015, *A&A*, 576, A107
- Popescu, C. C., Tuffs, R. J., Dopita, M. A. et al. 2011, *A&A*, 527, A109
- Pozzi, F., Calura, F., Zamorani, G. et al. 2020, *MNRAS*, 491, 5073
- Qin, J., Zheng, Z. X., Wuyts, S. et al. 2024, *MNRAS*, 528, 658
- Remy-Ruyer, A., Madden, S. C., Galliano, F. et al. 2013, *A&A*, 557, A95
- Rémy-Ruyer, A., Madden, S.C., Galliano, F., Galametz, M., Takeuchi, T. T. et al. 2014, *A&A*, 563, A31
- Rémy-Ruyer, A., Madden, S. C., Galliano, F. et al. 2015, *A&A*, 582, A121
- Saintonge A., Wilson, C. D., Xiao, T. et al., 2018, *MNRAS*, 481, 3497
- Salim, S., Rich, R. M., Charlot, S., et al. 2007, *ApJS*, 173, 267
- Shetty, R., Kauffmann, J., Schnee, S., Goodman, A. A. 2009, *ApJ*, 696, 676
- Shetty, R., Kauffmann, J., Schnee, S., Goodman, A. A. & Ercolano, B. 2009, *ApJ*, 696, 2234
- Skibba, R. A., Engelbracht, C. W., Dale, D. . et al. 2011, *ApJ*, 738, 89
- Smith, M. W. L., Eales, S. A., Gomez, H. L. et al. 2012, *ApJ*, 756, 40
- Somovigo, L. & Algera, H. 2025, *MNRAS*, 540, 3693
- Tabatabaei, F. S., Braine, J., Xilouris, E. M., et al. 2014, *A&A*, 561, A95
- Tang, Y., Wang, Q. D. & Wilson, G. W. 2021, *MNRAS*, 505, 2377
- Taylor, V., Casasola, V., Pozzi, F. et al. 2025, *A&A*, 701, A74
- van der Giessen, S. A., Leslie, S. K., Groves, B. et al. 2022, *A&A*, 662, A26
- Vlahakis, C., Dunne, L. & Eales, S. 2005, *MNRAS*, 364, 1253
- Weingartner, J.C. & Draine, B.T. 2001, *ApJ*, 548, 296
- Witstok, J., Jones, G. C., Maiolino, R. et al. 2022, *MNRAS*, 523, 3119
- Yang M., Phillips T. 2007, *ApJ*, 662, 284

This paper has been typeset from a  $\text{\LaTeX}$  file prepared by the author.